Research Article

Emergent Behavior in Oxidation Catalysis over Single-Atom Pd on a Reducible CeO₂ Support via Mixed Redox Cycles

Linxi Wang,[§] Shyam Deo,[§] Ahana Mukhopadhyay, Nicholas A. Pantelis, II, Michael J. Janik,* and Robert M. Rioux*

Read Online

| ACCESS | | Metrics & More | | Article Recommendations | | Supporting Information |

ABSTRACT: Experimental kinetics demonstrate catalytic lean CO oxidation over single Pd atoms with a CO reaction order greater than unity. A CO order greater than unity is unique to Pd single atoms supported on CeO₂ nanocubes and is not observed for Pd nanoparticles on the same support nor other supported single-atom systems. A reaction mechanism including eight elementary steps, in which Pd dynamically samples three formal oxidation states, is unable to capture a reaction order in CO greater than unity. Vibrational spectroscopy of CO adsorption ranging from lean to rich conditions reveals Pd accesses an extensive array of formal oxidation states, ranging from Pd^{4+} to Pd^0. Density functional theory calculations demonstrate

Pd atoms supported on CeO₂ can access four formal oxidation states during lean CO oxidation. Two catalytic redox cycles are possible, with cross-over between them leading to a reaction mechanism yielding reaction orders in CO greater than unity. A microkinetic model, utilizing Bayesian inference to adjust elementary energetics to fit the experimentally measured activation barrier and reaction orders, confirms the reaction order in CO of >1 arises from the ability of the Pd active site to access four formal oxidation states, spanning from +4 (PdO_2) to −2 (Pd adjacent to a CeO₂ lattice oxygen vacancy). This work demonstrates the emergent redox behavior of Pd single atoms on CeO₂, which may be important to explain their high activity for low-temperature catalytic combustion of hydrocarbons.

KEYWORDS: single atoms, palladium, oxidation, carbon monoxide, emergent behavior, redox
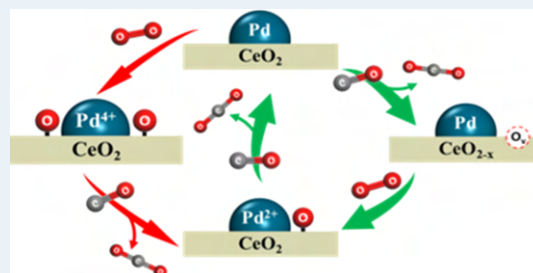
1. INTRODUCTION

Redox catalysis inherently involves participant metal atoms dynamically oscillating between various oxidation states. Facile changes in the oxidation state are crucial to high redox activity, and identification of the metal oxidation states involved in the redox cycle is necessary to explain observed kinetic behaviors and improve catalyst design. Dynamic variation in the metal oxidation states affects the reactivity and selectivity of extended metal surfaces,[1,2] supported metal nanoparticles (NPs),[3,4] and single-atom metal catalysts.[5−7] Daelman et al. performed density functional theory (DFT) and first-principles molecular dynamics simulations of supported Pt single atoms on CeO₂(100) surfaces and found several dynamically interconnected charge states.[5] Senftle et al. performed DFT calculations on hydrocarbon oxidation reactions over single-atom Pd/CeO₂ catalysts and attributed the high activity to the ability of Pd atoms to transition between Pd^{4+} and Pd^{2+} oxidation states, enabling rapid C−H activation on Pd-doped ceria catalysts.[8,9]

The oscillation between oxidation states is well appreciated in homogeneous catalysis, and reaction mechanisms attempt to precisely define various metal oxidation states within a redox cycle.[10−12] Zhang et al.[13] studied electrochemical water oxidation over Fe-based octahedral complexes where the oxidation state of the iron center is proposed to alternate

between III and V ($Fe^{III}(H_2O)^{2+}$ and $Fe^V(O)^{2+}$, respectively) twice during the catalytic cycle via an oxidative $2e^−/2H^+$ proton-coupled electron transfer reaction of $Fe^V(O)^{2+}$ with water. The catalyst oxidation state (III) regenerates through O₂ release. Heterogeneous catalysis over supported single metal atoms provides similar opportunities for the metal atoms to oscillate between different oxidation states. Identifying the oxidation states of metals in single-atom catalysts (SACs) during redox cycles is challenging. The support can be considered akin to a "ligand", but this is an imperfect analogy since a single metal atom has not only local electronic states but also delocalized states participating in the extended band structure of the oxide support.[14] Hence, the identification of the oxidation states of metal site(s) under dynamic conditions is crucial to determine the active species in SACs and to probe the role of the support in enabling emergent redox properties.
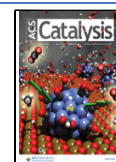
The bulk oxidation state of the metal in a supported catalyst is often assumed to be the active and dominant state throughout the reaction mechanism.[15] For a metallic NP catalyst, electronic states are delocalized,[16] and therefore, the binding of the adsorbate does not alter the formal oxidation state of the metal. For catalysis over metal oxides, delocalized states also participate in redox cycles,[16,17] and it is challenging to characterize the changes in local oxidation states within a relatively static extended oxide structure.[18–20] Late transition metal SACs have electrons both in localized d states and in delocalized states due to electronic interaction with the underlying oxide support and/or reactants, with the single atoms undergoing dynamic charge transfer between distinct oxidation states.[21] Moreover, the most populous oxidation state(s) under reaction conditions can differ with varied redox conditions (i.e., at room temperature in air vs at an elevated reaction temperature in a CO/O_2 mixture).[22] Dynamic changes in the oxidation state during catalytic cycles are typically short-lived and difficult to characterize.[23] The oxidation states determined by ex situ X-ray photoelectron spectroscopy (XPS) refer to the "resting states" of the metal species,[24] which do not necessarily represent the oxidation state experienced during reaction. The thermodynamic redox condition is also typically different in an XPS chamber than the reaction conditions. XPS results obtained under ex situ conditions may not provide an accurate picture of the surface active metal oxidation states during reaction. X-ray absorption spectroscopy analysis under in situ conditions is challenging due to the low signal-to-noise ratio as a result of the intrinsically low metal loading of metal-oxide-supported SACs.[25]

To investigate the in situ dynamic nature of oxidation states, CO oxidation is a useful probe reaction due to the simplicity of its reaction cycle and the intrinsic sensitivity of the bonded CO stretching vibrational mode to its local environment. CO bound to metal atoms at different oxidation states exhibits distinct C–O stretching frequencies due to different extents of CO-metal electronic back donation, altering the C–O bond strength. This convenient characterization technique provides opportunities for the in situ recording of dynamic oxidation states of supported single atoms in response to varying reaction conditions. DFT calculations revealed the coexistence of SACs in multiple oxidation states through the construction of reaction mechanisms that track oxidation states under different reaction conditions, and microkinetic modeling (MKM) accounted for the extent to which various reaction mechanism(s) contributed to the observed reaction kinetics.[21,26] DFT studies of CO oxidation over atomically dispersed Pd and Ir have shown that both CO oxidation (i.e., OC–O bond formation) and O_2 activation (i.e., O–O dissociation) occur local to the metal center.[27–29] This leads to a typical redox cycle in which one O atom reacts with CO, followed by the addition of two O atoms due to O_2 adsorption and dissociation, and then, the "extra" O is used to oxidize another CO, after which the active site returns to its original oxidation state. The elementary steps for this basic CO oxidation mechanism over a Pd single-atom site (noted as PdO_x) with an unspecified initial oxidation state are summarized in Table 1. In this scenario, Pd oscillates among three oxidation states (PdO_x, PdO_{x-1}, and PdO_{x+1}) during the catalytic cycle. The value of x represents the middle oxidation state of Pd in the cycle, with plausible values of $x = 1$ (allowing Pd to oscillate between +4, +2, and 0 formal oxidation states during the catalytic cycle) or $x = 0$ (in which Pd transits between PdO, Pd^0, and Pd with an O vacancy in the support). Although the number of O atoms may be used to assign a formal oxidation state to Pd

Table 1. Elementary Steps for a Dual Oxidation Cycle of a PdO_x Site Converting CO to CO_2 Over a Redox-Active Support[a]

step no	elementary step	reaction
1	1st CO adsorption	$PdO_x + CO_{(g)} \leftrightarrow CO\text{--}PdO_x$
2	1st CO Oxidation to CO_2 (OC–O)	$CO\text{--}PdO_x \leftrightarrow CO_2\text{--}PdO_{x-1}$
3	1st CO_2 desorption	$CO_2\text{--}PdO_{x-1} \leftrightarrow CO_{2(g)} + PdO_{x-1}$
4	O_2 adsorption	$PdO_{x-1} + O_{2(g)} \leftrightarrow (O_2\text{--}PdO_{x-1})$
5	O_2 dissociation	$(O_2\text{--}PdO_{x-1}) \leftrightarrow PdO_{x+1}$
6	2nd CO adsorption	$PdO_{x+1} + CO_{(g)} \leftrightarrow CO\text{--}PdO_{x+1}$
7	2nd CO Oxidation to CO_2 (OC–O)	$CO\text{--}PdO_{x+1} \leftrightarrow (CO_2\text{--}PdO_x)$
8	2nd CO_2 desorption	$(CO_2\text{--}PdO_x) \leftrightarrow CO_{2(g)} + PdO_x$

[a]A "–" is used to separate an adsorbate from its adsorption site. O atoms consumed during CO oxidation steps or added during re-oxidation by O_2 may be directly associated with Pd atoms or within the CeO_2 support.

atoms, a reducible support (i.e., CeO_2) may alter the effective formal oxidation states of Pd due to the oscillation of support metal (Ce) atoms (between Ce^{4+} and Ce^{3+}) during the redox cycle. Therefore, the 8-step mechanism of CO oxidation in Table 1 may be an oversimplification since Pd atoms can span beyond three oxidation states (by coupling the mechanisms with $x = 0$ and 1) or involve "non-local" reaction processes through the diffusion of O atoms within Pd/CeO_2.

We combine experimental kinetic studies, vibrational spectroscopy, DFT calculations, and MKM to evaluate the elementary mechanisms of CO oxidation over Pd/CeO_2 SACs. We supported Pd single atoms on ceria nanocubes with exposed (100) facets to reduce the heterogeneity of local Pd environments. Kinetic studies reveal a unique behavior of Pd single atoms characterized by a reaction order of CO greater than unity. Diffuse reflectance infrared spectroscopy (DRIFTS) is used to examine the accessible oxidation states of Pd single atoms during redox processes. DFT calculations are used to construct reaction mechanisms with energetics consistent with experimentally measured kinetic parameters. MKM, together with Bayesian inference, is used to evaluate whether a reaction mechanism is consistent with observed experimental kinetics. Combination of the experimental and computational results leads to the conclusion that Pd single atoms can access PdO_2, PdO, Pd, and Pd–O vacancy ($Pd\text{--}O_v$) configurations during the reaction cycle, and the dynamic variation among these oxidation states contributes to oxidation catalysis on Pd/CeO_2. This unique behavior emerges from the $Pd\text{--}CeO_2$ interaction, allowing Pd to reach the highly oxidized 4+ oxidation state due to the reducibility of the support. Collectively, the observed CO oxidation kinetic behavior differs from Pd NPs because the strong $Pd\text{--}CeO_2$ interaction enables Pd to access multiple oxidation states, leading to mixing between distinct Pd redox cycles.

2. EXPERIMENTAL AND COMPUTATIONAL METHODS

2.1. Synthesis of CeO_2 Nanocubes and Single-Atom Pd/CeO_2 Catalysts. CeO_2 nanocubes were synthesized by a hydrothermal reaction following the method of Zhao and Wang et al.[30,31] In a typical synthesis, $Ce(NO_3)_3\cdot6H_2O$ (2.71 g) (Sigma Aldrich) was dissolved in 5 mL of deionized (DI) water in a Teflon container. NaOH (30 g, solid pellets) was dissolved in 120 mL of DI water, and the NaOH solution was added

dropwise to the Teflon container over a period of 15 min, during which the initially transparent solution turned yellow, followed by purple. After the complete addition of NaOH, the stir bar was removed, and the Teflon container was capped and placed in an autoclave held at 180 °C for 24 h. The autoclave was removed and cooled to room temperature in a cold water bath. CeO_2 precipitates were collected after centrifugation of the suspension. The precipitates were washed with DI water and ethanol three times each and dried overnight at 105 °C. We calcined the CeO_2 product in dry air (100 sccm) at 400 °C for 4 h to obtain the final nanocubes. The structure of the CeO_2 nanocubes was characterized by transmission electron microscopy (TEM), which demonstrated the formation of CeO_2 nanocubes exposing (100) facets.

The Pd/CeO_2 catalysts were prepared by the strong electrostatic adsorption method.[32,33] All reported Pd loadings are on a weight basis. Tetraamine palladate chloride (Pd-$(NH_3)_4Cl_2$, Alfa Aesar, 99.9%) was used for all syntheses. Calculated amounts of the Pd precursor to achieve the desired weight loading were dissolved in 10 mL of DI water, and the pH of each solution was adjusted to 11. For catalysts with low Pd weight loadings (<0.2%), an ammonia solution was used for pH adjustment to prevent the introduction of other possible metal ions. For catalysts with higher Pd weight loadings (>0.4%), we found it difficult to reach target Pd loadings using an ammonia solution, and NaOH solution was used for final pH adjustment. After stabilization of the pH of the Pd solution, a calculated amount of ceria support was added. The addition of the support decreased the pH values due to the adsorption of hydroxide anions on the CeO_2 surface, and an additional base was added to return the pH to 11. The suspension was stirred with continuous pH monitoring for ~1 h to allow adsorption of Pd cations onto the charged surface of the CeO_2 support. The suspension was then filtered, washed with 10 mL of DI water three times, and dried overnight at 105 °C, followed by calcination in dry air (Praxair, Ultra Zero Air) at 400 °C for 4 h.

2.2. Characterization of the CeO₂ Support and Pd/CeO₂ Catalysts. The synthesized CeO_2 nanocubes were characterized by volumetric adsorption, TEM, and X-ray diffraction (XRD). For TEM characterization, a small amount of CeO_2 nanocubes was dispersed in 10 mL of ethanol and sonicated to obtain a uniform suspension. A drop of this suspension was added to a lacey carbon-coated copper grid. Imaging and elemental mapping were carried out using a FEI Talos F200X microscope with a field emission source operating at an accelerating voltage of 200 kV in both TEM and STEM modes. Metal NPs/atoms supported on the ceria support were imaged using a FEI Titan³ G2 microscope at an accelerating voltage of 200 kV.

Powder XRD measurements were performed using a Malvern Panalytical XPert Pro MPD $\theta-\theta$ diffractometer operating in the $\theta-2\theta$ Bragg configuration using Cu Kα ($\lambda = 1.5406$ Å) radiation at 40 kV. Scans were made from 20 to 80° with a step size of 0.02° at a scan rate of 4°/min. Surface measurements determined by Kr adsorption at 77 K on a Micromeritics 3FLEX volumetric adsorption apparatus demonstrated a surface area of 10–11 m² g⁻¹ for the calcined cubes. The change in surface area upon the addition of Pd up to 1 wt % was negligible.

Inductively coupled plasma–optical emission spectrometry (ICP–OES) (Agilent ICP–OES 700) was applied to determine the total metal content adsorbed on the surface of the support. Approximately 10–100 mg of catalysts (dependent on the Pd weight loadings) were added to a 20 mL scintillation vial along

with aqua regia (1 mL of fuming HNO_3 and 3 mL of saturated HCl) to dissolve Pd. The vial was capped and left to stand for 2 h, followed by the addition of 4 mL of DI water to dilute the acid solution. To avoid introduction of CeO_2 NPs into the ICP–OES, the suspension was collected by a 5 mL syringe and injected into another vial through a syringe filter (Restek, O.D. = 25 mm, 0.22 μm porosity). Standard solutions with appropriate Pd contents were prepared by diluting a stock Pd (100 μg/mL) calibration standard purchased from Inorganic Ventures (Christiansburg, VA) to construct a calibration curve for quantitative Pd determination.

2.3. Kinetic Measurements of CO Oxidation on Pd SACs. Kinetic measurements were conducted in a home-built, down-flow fixed-bed reactor (Figure S1). Pd/CeO_2 catalysts (5–30 mg, dependent upon the Pd weight loading) were weighed and mixed with silicon carbide (SiC) to make a total sample bed of ~100 mg. SiC increased the thermal conductivity of the bed to avoid a local temperature increase due to exothermic reaction. The reactor was heated by a slow ramp rate (~3 °C/min) to target temperatures under He flow (30 mL/min). After the temperature stabilized, the He flow was switched to CO/O_2/He flow at the same total flow rate to initiate CO oxidation. The bed was loaded in a quartz tube (1/2″ O.D.) and fixed between two pieces of calcined quartz wool. A K-type thermocouple inserted into the tube was in direct contact with the catalyst bed. Effluent gases were quantified with a HP 5890 Series II gas chromatograph outfitted with a thermal conductivity detector (TCD). A ShinCarbon ST micro-packed GC column (Restek Corporation, Bellefonte, PA) was used to separate gaseous components. Helium was used as a carrier gas through the column. The gas injections are made using a 10-port valve via a sample loop injection system. Before measurements, the GC signals were calibrated using 2–10% CO/He and 0.1–0.5% CO_2/He gases to determine the TCD response factor for CO and CO_2. The activation energy of CO oxidation on each sample was determined from Arrhenius plots comprised of five different temperatures, while CO and O_2 reaction orders were determined by reaction order plots at five different CO and O_2 partial pressures, respectively. The temperatures and pressures were varied within a small range in random order to eliminate systematic measurement errors. After the collection of five data points in each set of measurements, the first data point was repeated to ensure data reproducibility. The conversion of CO was limited to <10% for all reaction conditions examined, and all reported rates were calculated assuming differential reactor operation. Kinetic data was collected for ~2 h at each condition, with data from approximately the last 10 min averaged to report a steady-state rate (deactivation under the lean reaction conditions was minimal over this time frame). Under any set of reaction conditions, rates varied by less than 10% for all samples (from the same batch of catalysts).

2.4. In Situ CO-DRIFTS Measurements. In situ DRIFTS measurements were conducted on a Bruker Vertex 80v FTIR spectrometer coupled with a Praying Mantis diffuse reflection accessory and a high-temperature reaction chamber (Harrick Scientific). Three gases including 5% CO/He (Research Grade, Praxair), helium (UHP, Praxair), and 25% O_2/He (UHP, Praxair) were used as received. In a typical experiment, a calcined catalyst (~60 mg) was added to the reaction chamber, purged with He at 200 °C for 30 min, and then cooled to the adsorption temperature; a DRIFT spectrum was recorded under He. This spectrum served as a reference for the subtraction of background features associated with the ceria support. During
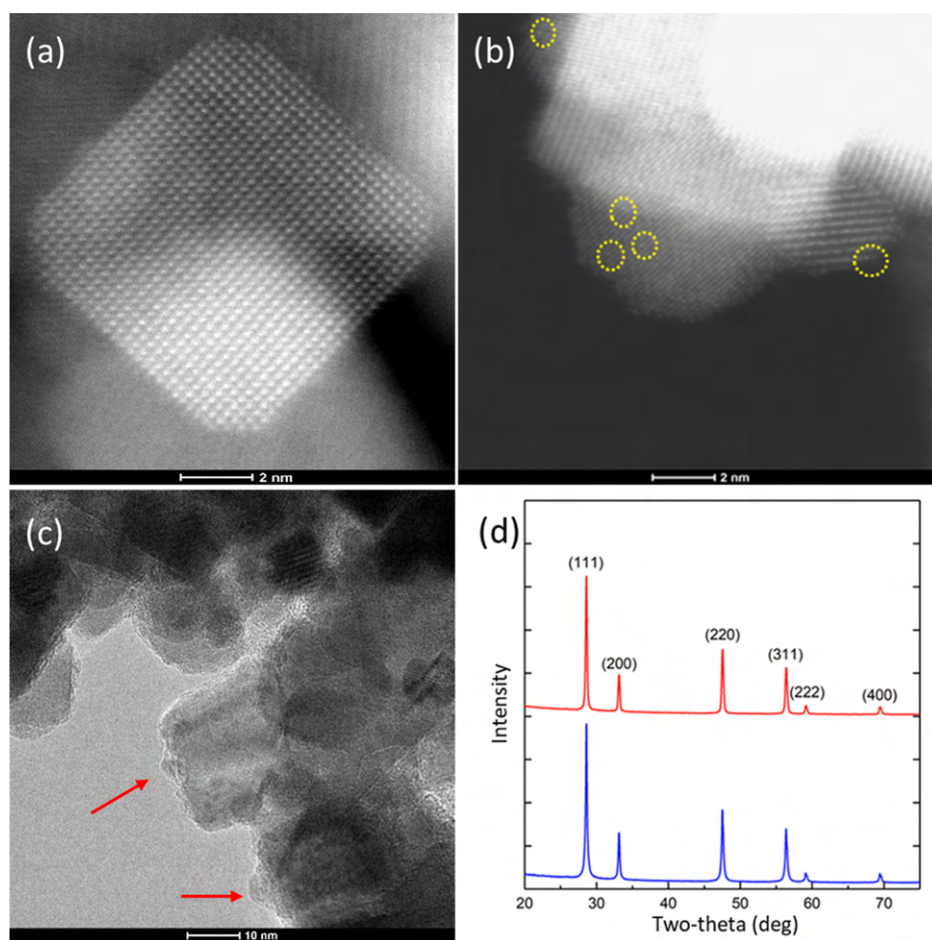
Figure 1. HR-STEM image of (a) CeO_2 nanocubes and STEM images of the synthesized (b) 0.05% Pd/CeO_2 catalysts with Pd single atoms indicated by yellow dashed circles; (c) 1% Pd/CeO_2 with Pd NPs marked by red arrows; and (d) XRD spectra of the (blue) CeO_2 support and the (red) 0.05% Pd/CeO_2 catalyst.

DRIFTS measurements of CO adsorption, gases were mixed in a manifold and introduced to the reaction chamber. Volumetric flow rates of gases were adjusted with needle valves attached to rotameters to achieve different partial pressures of CO required for the IR spectroscopy experiment—CO adsorption, pressure-swing desorption, temperature-programmed desorption, and catalytic CO oxidation. To record the change in surface chemistry during in situ measurements, time-resolved scans were collected every 5 to 10 min. For each spectrum, 100 scans were averaged to increase the signal-to-noise ratio.

2.5. Computational Methods. *2.5.1. Density Functional Theory.* DFT calculations are used to identify plausible atomistic structures of Pd/CeO_2 (100) catalysts, probe CO adsorption energetics, and vibrational frequencies as a function of the PdO_x oxidation state and provide plausible reaction energetics for CO oxidation catalytic cycles. Spin-polarized plane-wave DFT calculations were carried out using the Vienna ab initio simulation package (VASP), version 5.4.4.[34,35] The electron exchange and correlation energies were computed using the Perdew, Burke, and Ernzerhof version of the generalized gradient approximation (GGA) functional.[36] The projector augmented-wave (PAW)[37] method was used to represent the ion-core electron interactions. The cerium 5s, 5p, 5d, 4f, and 6s electrons, the oxygen 2s and 2p, and the Pd 4d and 5s electrons were treated as valence electrons. The structural convergence criteria for forces were 0.05 eV Å^{-1} for all unconstrained atoms.

The DFT + U method[38] within VASP was used for Ce f states with a U_{eff} value of 5 eV to correct for on-site coulombic interaction, as recommended by Nolan et al.[39] A plane-wave energy cutoff of 500 eV was used to represent the valence electrons, and a Monkhorst−Pack[40] k-point mesh of $3 \times 3 \times 1$ was used with the third vector perpendicular to the ceria (100) surface (Figure S2). Transition states (TS) were located using the climbing image nudged elastic band (CI-NEB) method[41] (5−7 images) and the dimer method[42] by relaxing the forces below 0.05 eV Å^{-1} and further confirmed through the presence of a single imaginary frequency along the reaction coordinate. Vibrational frequencies were calculated using partial Hessian analysis via numerical second derivatives with displacements of 0.01 Å. The complete methodology is detailed in Supporting Information Section S2.

The CeO_2 (100) surface was modeled as a slab of cubic fluorite. The optimized bulk CeO_2 equilibrium lattice parameter of 5.481 Å is consistent with the experimental value of 5.411 Å.[43] A $p(4 \times 4)$ expansion of the surface unit cell was used, and a checkerboard surface structure (where only half of the surface oxygen atoms are located on one (100) surface and the other surface oxygen atoms on the opposite (100) surface[44]) was used to remove the permanent dipole of the (100) surface. Further details of the surface slab construction and adsorption of Pd single atoms, including images of structures, are included in Section S2.1 (Figures S2−S6). Adsorption energies, reaction

energies, activation barriers, and oxygen vacancy formation energies follow their typical definitions, as detailed in Supporting Information Sections S2.2–2.4 (Figures S7). The oxidation states of Pd SACs are determined as detailed in Section S2.5 (Figure S8).

2.5.2. Microkinetic Modeling (MKM) and Bayesian Inference Approaches. MKM was used to evaluate the ability of individual elementary reaction mechanisms to yield kinetic behavior consistent with experiments. Although agreement with the experiment cannot prove a mechanism, MKM proves useful in this study to examine the requirements of a mechanism to match experimental observables (activation barrier and reaction orders). Elementary adsorption, desorption, and surface reaction rate constants were written using TS theory formalisms detailed in Section S2.6. An in-house Python code was used to evolve the surface coverage of species to a steady state given a set of reaction energetics and reaction conditions (CO, O_2, pressure, and temperature). Activation barriers were calculated from the MKM by varying the temperature and then fitting the reaction rates to the Arrhenius equation. Reaction orders with respect to a species (CO or O_2) were calculated by varying the species' partial pressure and recording the corresponding reaction rates.

DFT provided initial elementary reaction energies and activation barriers for all elementary steps. However, these energetics are not expected to quantitatively match the experimentally observed kinetics due to their reliance on a specific single site model (perfect CeO_2 (100) surface, single site of adsorption for PdO_x species, etc.) along with errors associated with exchange−correlation functions for such highly correlated systems.[45,46] As such, a Bayesian inference-based statistical approach[47] was used to adjust elementary energetics in order to fit the experimentally measured activation barrier and reaction orders. The complete computational approach to MKM and Bayesian inference is detailed in Sections S2.6 and 2.7.

3. RESULTS AND DISCUSSION

3.1. Structural Characterization of Pd/CeO₂ Catalysts. The dispersion of Pd at different weight loadings on CeO_2 was characterized by HR-STEM, XRD, and kinetic methods. CeO_2 nanocubes have a dimension of ~20 ± 5 nm (Section S3 and Figure S9) and expose (100) facets (Figure 1a). As demonstrated in Figure 1b, the STEM image of the 0.05% Pd/CeO_2 catalyst showed only Pd single atoms on CeO_2 nanocubes without any observable Pd NPs. By comparison, the formation of Pd NPs is easily observed (Figure 1c) at a loading of 1% Pd. The XRD spectra of the 0.05% Pd/CeO_2 and CeO_2 support are illustrated in Figure 1d. Diffractograms revealed the structure of CeO_2 crystals lacked any features associated with Pd.

We measured rates for the oxidation of CO at different Pd weight loadings and calculated the specific activity of the Pd/CeO_2 catalysts to differentiate between single atoms and NPs. It is reasonable to assume atomic dispersion of Pd at the lowest weight loading (0.0036%) since the TEM imaging of the 0.05% Pd/CeO_2 identified Pd to be only present as a single atom. The specific activity [$mmol_{CO2}$/s-g_{cat}] is plotted against Pd weight loading in Figure 2. At low weight loadings, the rate is proportional to the amount of deposited Pd, which suggests that the metal efficiency is at maximum and all Pd sites are equally active. The average activity of the Pd sites is illustrated by turnover frequencies (TOFs, defined as the number of molecules reacted per Pd atom per second), which fall within
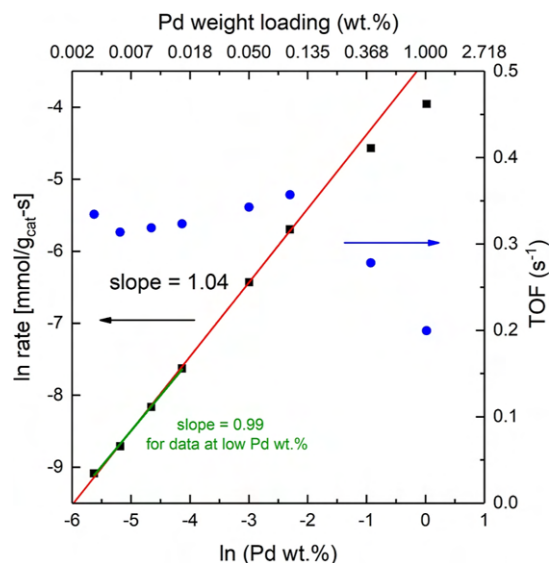
Figure 2. Natural logarithm of specific activity (■) and calculated TOFs (●) plotted against the natural logarithm of Pd weight loadings assuming all Pd is atomically dispersed. The measurements were conducted at 200 °C with the feed consisting of 2% CO and 20% O_2 in balance He. The green line is the linear fit of the data points at the lower end of Pd weight loadings. The upper x-axis indicates the corresponding Pd weight loadings.

a small range (0.31−0.35 s^{-1} at 200 °C) for Pd weight loadings less than 0.15%. As the Pd weight loading further increases, the measured rate continues to increase, but the TOF drops. This suggests a decreased metal efficiency of Pd due to the formation of Pd nanoclusters. Assuming all Pd is available for reaction, the calculated TOFs drop significantly at high Pd weight loadings (>0.39%), implying that the number of active sites declines due to the formation of NPs. We conclude that the clustering of single atoms to NPs occurs at a Pd weight loading between 0.12 and 0.39%. Approximate analysis for the number of Pd atoms deposited per ceria cube (20 ± 5 nm edge length) confirms Pd atoms remain sufficiently spaced to retain atomic dispersion until loadings of 0.1% by weight (Section S4 and Figure S10 and Table S1). The average spacing between the adjacent Pd atoms at this weight loading was calculated to be 0.125 Pd atoms per nm^2 of the CeO_2(100) surface if all the Pd atoms are dispersed over the flat CeO_2 terrace surfaces. The spacing is 1 Pd per 0.5 nm of the edge if all Pd atoms are deposited over the edges of the ceria nanocubes.

3.2. DFT Model Development for CO Adsorption to PdOₓ/CeO₂ (100). We used DFT calculations to examine the redox and CO adsorption properties of PdO_x (x = 0, 1, 2) species adsorbed on the CeO_2 (100) surface. PdO_x species favor adsorption on a bridge site between two surface oxygen atoms (Figure S4). The oxygen adsorption energy, relative to gas-phase O_2, is favorable both to convert Pd to PdO (−0.83 eV) and to convert PdO to PdO_2 (−1.21 eV). The oxidation of CO could lead to the formation of O vacancies in the CeO_2 (100) surface. In the reduction direction, Pd adsorption makes the oxygen vacancy formation energy (for the O nearest to Pd) more endothermic, at 2.52 eV compared to 1.50 eV for the bare CeO_2 (100) surface. Section S5 (Tables S2−S8) reports the redox energetics, spin states, and formal oxidation states across the PdO_x/CeO_2 (100) models. The method to assign oxidation states for PdO_x on CeO_2 (100) is described in Section S2.5.

Oxidation states of adsorbed Pd atoms in Pd, PdO, and PdO_2 states are 0/+1 (energetically equal), +2, and +4, respectively.

We explored the impact of U_{eff} corrections to Pd 4d states on the adsorption energy of oxygen (Table S5). The energy to adsorb $1/2 O_2$ on Pd varies by 0.33 eV as the value of U_{eff} varies from 0 to 7 eV. This variance may be meaningful to Pd adatom redox catalysis and demonstrates absolute values of redox energetics for such strongly correlated systems will have an error at the GGA theory level that is challenging to quantify.

The adsorption energy of CO to PdO_x/CeO_2 (100) sites is dependent on the oxidation state of Pd (Table S3). The CO adsorption energies over Pd, PdO, and PdO_2/CeO_2 (100) are −1.04, −1.95, and −0.10 eV, respectively. The CO adsorption energy on Pd depends significantly on both the value of U_{eff} of Pd d (Table S6) and Ce f states (Table S7). The adsorption energy of CO to PdO_x/CeO_2 (100) is also dependent on the ceria model (Table S8). CO adsorption energies to a Pd atom adsorbed to stepped (Figure S5) and doped (cation substituted into the Ce lattice, Figure S6) ceria models are −1.27 and −0.91 eV, respectively, demonstrating the dependence of CO adsorption energy on the local Pd/CeO_2 (100) structure.

Collectively, we conclude Pd single atoms adsorbed on CeO_2 can likely access multiple oxidation states and show favorable CO adsorption. Both oxygen and carbon monoxide adsorption energies vary with the U_{eff} correction applied to Ce f and Pd d states, as well as between models of the Pd atom as a terrace adatom, step-adsorbed atom, or cation substituted into the Ce lattice. Quantitative DFT values for CO oxidation energetics cannot be relied on to provide precise agreement with experimental values, even for low Pd loadings on the nanostructured CeO_2 cubes.

3.3. Kinetics of CO Oxidation.
We measured apparent activation energies for the oxidation of CO on Pd/CeO_2 catalysts with various weight loadings. As shown in the Arrhenius plot (Section S6 and Figure S11), the inclusion of Pd decreases the apparent activation energy by ~15 kJ/mol compared to the pristine CeO_2 support. Apparent activation energy values fall within a narrow range (60−67 kJ/mol, Table 2) for all Pd/CeO_2 catalysts with weight loadings spanning from 0.0056 to 1%. Values reported on metallic Pd surfaces[48] and Pd deposited on inert supports[49,50] are in the range of 71−122 kJ/mol, suggesting synergy between the Pd metal sites and active CeO_2 supports.[51,52]

Reaction rates with varying CO and O_2 pressures for select catalysts are plotted in Figure 3, with a compilation of reaction orders for all catalysts included in Table 2. The reaction order in CO is sensitive to the Pd weight loading. At a high weight loading of Pd (1%), the CO order is slightly negative (−0.17), while the O_2 order is 0.16, which suggests CO poisons the Pd NPs due to the strong binding between CO and Pd. A positive reaction order in O_2 suggests Pd sites are largely covered by CO. Similar values of reaction orders were reported by Lang et al. on Pd NPs supported on CeO_2−ZrO_2, where the reaction is approximately zero order in CO and 0.3 with respect to O_2.[53] The measured reaction orders are in good agreement with previously reported values over Pd NPs on active supports (CeO_2, ZrO_2, and Fe_3O_4), where the CO order spans from −1 to 1 and the O_2 order from 0 to 1, both of which are dependent on the size of Pd NPs.[54] On the 0.12% Pd/CeO_2 catalyst, the reaction is first order in CO. A reaction order in CO near one has also been observed on single-atom $Ir/MgAl_2O_4$ catalysts, indicating reaction mechanisms differ between single atoms and NPs.[28] A positive reaction order in CO suggests Pd SACs

Table 2. Reaction Orders of CO and O_2 and Apparent Activation Energy on Pd/CeO_2 Catalysts with Different Pd Weight Loadings

Pd wt %	temperature (°C)	CO order[a]	O_2 order[b]	apparent E_a (kJ/mol)[c]
0.0056	200	1.30	−0.13	66.4
0.01	200	1.33	−0.20	66.2
0.016	200	1.30	−0.17	65.1
0.03	160	1.25	−0.1	62.4
0.051	150	1.19	−0.09	63.8
0.12	120	1.01	−0.02	65.2
0.40	120	0.22	0.10	60.5
1.02	120	−0.17	0.16	64.1

[a]CO reaction orders were measured at a total gas pressure of 101.3 kPa. The O_2 partial pressure was fixed at 20 kPa, and the CO partial pressure was varied between 2 and 10 kPa, respectively. [b]O_2 reaction orders were measured at a total gas pressure of 101.3 kPa. The CO partial pressure was fixed at 6 kPa, and the O_2 partial pressure was varied between 10 and 30 kPa, respectively. [c]The Arrhenius plot of CO oxidation was measured at a total gas pressure of 101.3 kPa. The CO and O_2 partial pressures were 2 and 20 kPa, respectively, and the temperature was varied from 120 to 220 °C. The temperature range depended on the Pd weight loading.
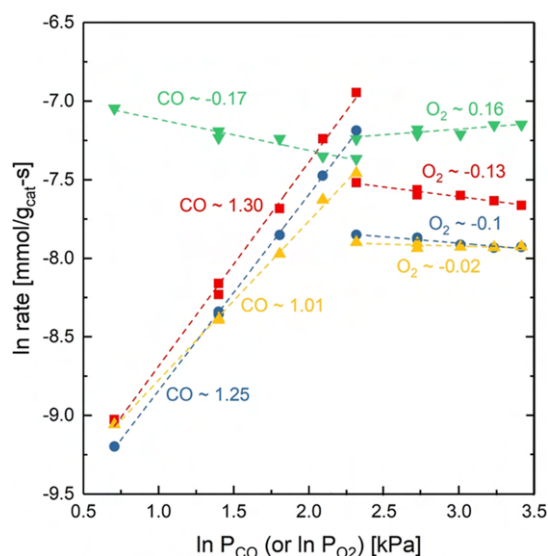
Figure 3. Reaction orders in CO and O_2 for CO oxidation on (■) 0.0056% Pd/CeO_2 at 200 °C, (●) 0.03% Pd/CeO_2 at 150 °C, (▲) 0.12% Pd/CeO_2 at 120 °C, and (▼) 1% Pd/CeO_2 at 120 °C. For the measurement of CO reaction orders, the O_2 partial pressure was fixed at 20 kPa and the CO partial pressure was varied between 2 and 10 kPa, respectively. For the measurement of O_2 reaction orders, the CO partial pressure was fixed at 6 kPa and the O_2 partial pressure was varied between 10 and 30 kPa, respectively.

are not saturated with CO during steady-state catalysis. On the 0.12% Pd/CeO_2 catalyst, the reaction order toward O_2 is nearly zero, suggesting limited involvement of O_2 in any rate-determining elementary reaction.

As the Pd weight loading further decreases, the reaction becomes greater than first order in CO, which has also been reported by Muravev et al.[55] This uncommon kinetic behavior implies distinct chemical properties of the supported single Pd atoms, which we will conclude with DFT calculations and MKM is due to a wide variation of Pd oxidation states during catalytic turnover. Alexopoulos and Vlachos proposed an adsorption

model of CO on alumina-supported SACs where each metal site can bind up to two CO molecules, both of which can be oxidized. Their MKM demonstrated the CO order could span from −1 to nearly 2, though, in their model, reaction orders greater than unity are only possible if the Pd site binds a pair (dicarbonyl) of CO molecules.[56] However, we rule out the possibility of Pd-dicarbonyl species as they are generally unstable,[57] especially at the high temperature (200 °C) used for our reaction order measurements. The Pd-dicarbonyl structure is also unsupported by our DRIFTS results, as noted in the next section, which showed only a single peak for adsorbed CO on Pd single atoms, while a dicarbonyl structure would exhibit two distinct vibrational bands attributed to symmetric and asymmetric vibrational modes.[28,58−60] A reaction order greater than one implies a more complex catalytic mechanism than the dual oxidation mechanism from Table 1, as discussed further in Section 3.5. Reaction orders in Figure 3 and summarized in Table 2 were collected at different temperatures to ensure that the reported kinetics were measured under differential conditions. Temperature was used to limit CO conversion over similarly composed catalyst beds, with Pd loadings varying by an order of magnitude. We conducted reaction orders in both CO and O_2 over the 0.0056% Pd/CeO_2 (single atom) at 220 °C and determined reaction orders of 1.32 in CO and −0.10 in O_2, demonstrating their insensitivity to temperature over a narrow range.

3.4. In Situ CO-DRIFTS Measurements for Single-Atom Pd/CeO_2.

The vibrational frequency of adsorbed CO is highly sensitive to the binding geometry and oxidation state of the Pd site.[61,62] We performed DRIFTS measurements of CO adsorption on a representative 0.03% Pd/CeO_2 sample at varying gas-phase compositions and temperatures. Figure 4a is the spectra of adsorbed CO on a calcined sample after exposure to CO adsorption, followed by a He purge at 25 °C and on a separate sample from the same batch of catalyst, following in situ reduction of CO at 100 °C, cooling to 25 °C, and a He purge at 25 °C. The infrared spectra of CO adsorbed on CeO_2 are featureless from room temperature up to 100 °C (the same temperature range examined with DRIFTS for Pd/CeO_2 catalysts). Detailed pretreatment procedures are included in Section S7. The spectrum of the calcined sample possesses a single CO-associated band at 2147 cm^{-1} after a He purge. Adsorbed CO bands near this position have been observed on PdO surfaces and supported Pd NPs on Al_2O_3 and CeO_2.[61,63−65] The single peak attributed to the adsorbed CO confirms the absence of Pd-dicarbonyls since a dicarbonyl species has a pair of vibrational bands in the DRIFT spectrum.[28,58−60] The spectrum of the CO-reduced sample has peaks associated with CO bound to Pd in a range of oxidation states, with the most prominent features at 2147, 2105, 2093, and 2070 cm^{-1}. Peaks associated with CO bridge-bonded or threefold coordinated to Pd NPs are observed in the 1800−2000 cm^{-1} region.[61,63] Although the exact Pd oxidation state attributable to each of these peaks is challenging to determine, we provide assignments in Section S8 (Table S9) based on prior literature and our calculated DFT adsorption frequencies. Harmonic frequencies were calculated with DFT for CO bound to PdO_x/CeO_2 (100) models (Table S3). The range of DFT-calculated frequencies generally matched the overall range of CO adsorption peaks in the DRIFTS spectra, supporting peak assignments to Pd single atoms in multiple oxidation states.

CO-DRIFTS results suggest a significant fraction of single Pd atoms are present in a highly oxidized state following calcination,
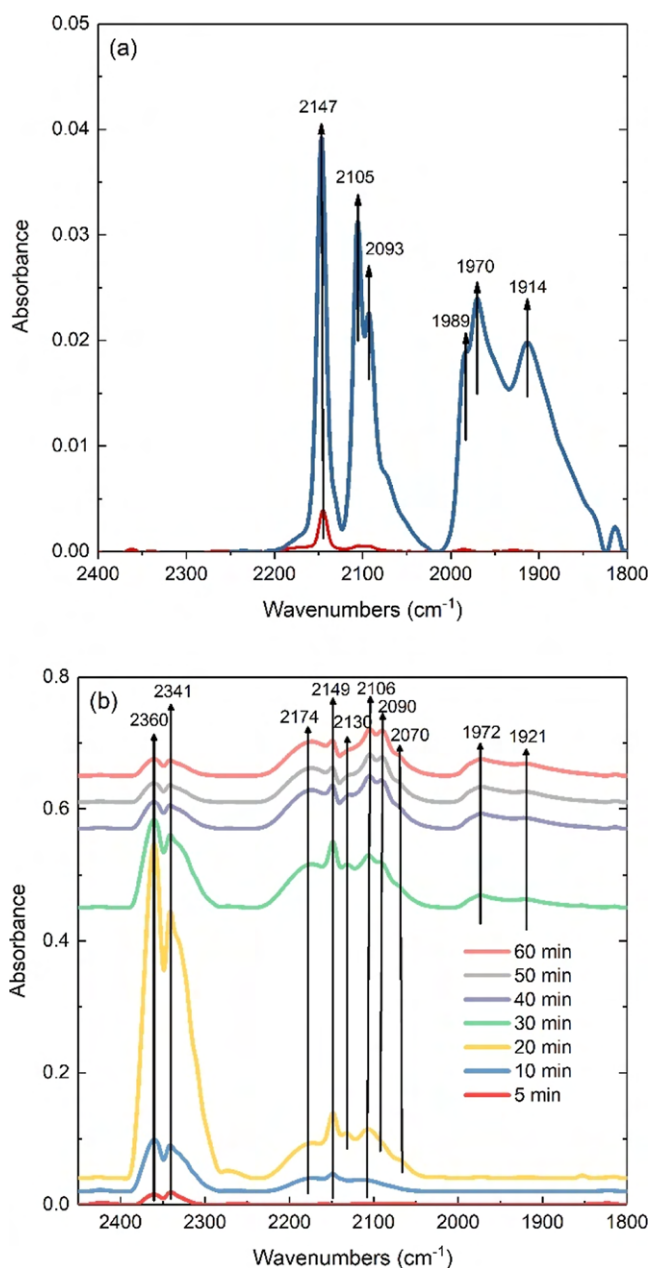
Figure 4. (a) DRIFT spectra of adsorbed CO on 0.03% Pd/CeO_2 after (red) CO adsorption at 25 °C for 60 min, followed by a He purge at 25 °C for 60 min, and (blue) in situ reduction in 5% CO/He at 100 °C for 60 min, cool down to 25 °C, and a purge in He at 25 °C for 60 min. (b) Time-resolved spectra during reduction of the 0.03% Pd/CeO_2 sample in 5% CO/He at 100 °C.

to which the adsorption of CO is weak. The CO adsorption peak observed at 2147 cm^{-1} for the calcined sample is relatively low in intensity compared to the same peak in the in situ-reduced sample, suggesting the fraction of Pd species with adsorbed CO increases the following reduction of CO at 100 °C. The 2147 cm^{-1} peak has previously been assigned as a $CO-Pd^{4+}$ state by Spezzati et al.,[66] although we find assignment to a $CO-Pd^{2+}$ state more consistent with both literature assignments and our DFT calculations.[61,64,67] Following calcination under dry air, a large fraction of the Pd single atoms are likely Pd^{4+} species, which is not detectable in the DRIFTS spectra due to weak $CO-Pd^{4+}$ binding. Our DFT calculations demonstrate CO adsorption to PdO_2/CeO_2 (100) sites is weak (−0.10 eV) and
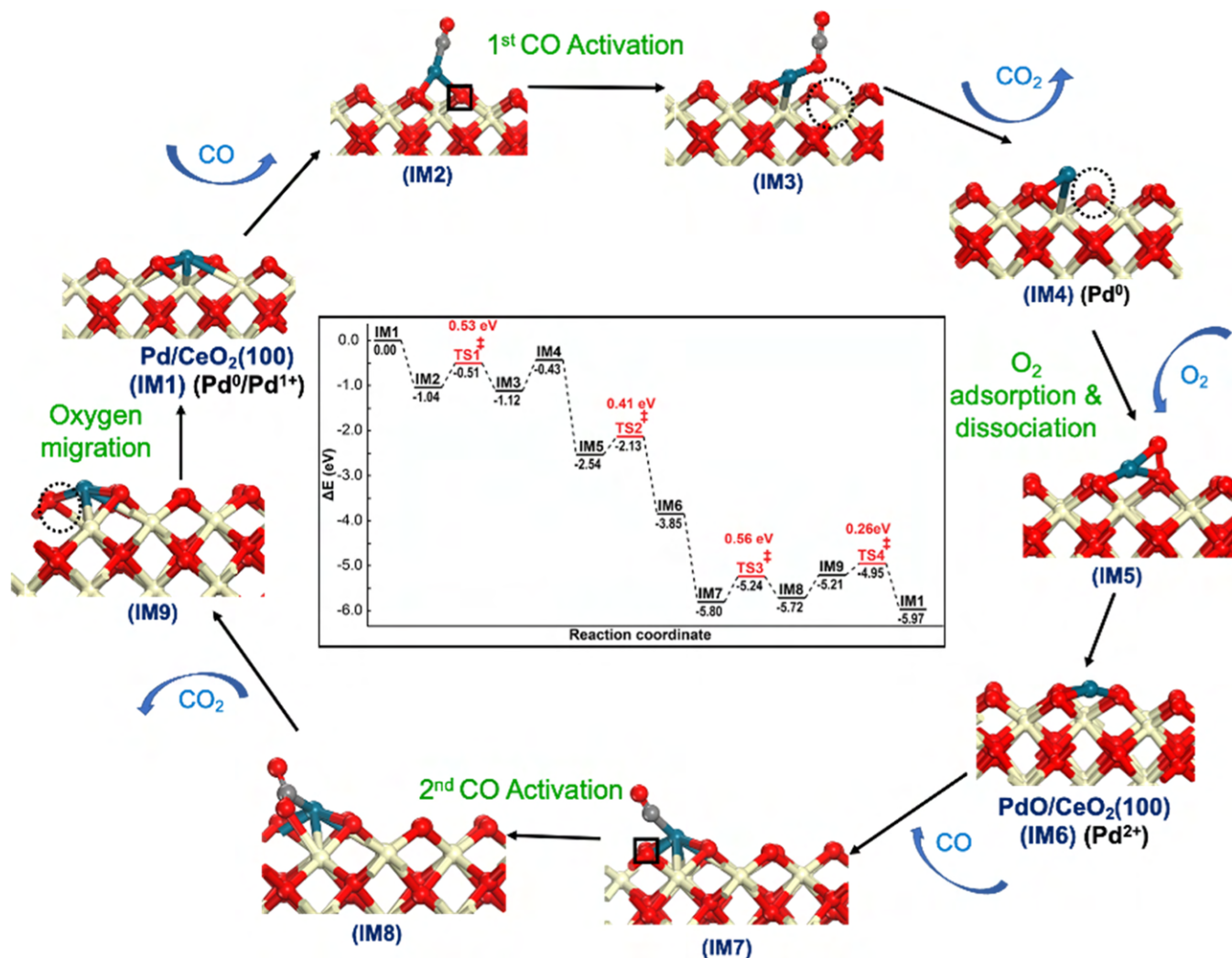
Figure 5. Pd redox cycle (Pd ↔ Pd–O_{vac} ↔ PdO ↔ Pd) and reaction energy diagram containing reaction energetics and activation barriers for the elementary steps with intermediate structures (IM1–IM9) and TS states (TS1–TS4). The TS structures are included in Table S11. Reaction energies and barriers for all the elementary steps are tabulated in Table S10. The O atoms in black squares indicate the O atoms involved in the activation of CO. The dashed circles indicate an oxygen vacancy formed during CO oxidation. Pd^{n+} indicated for PdO_x states represents the formal oxidation state of Pd, assigned based on determining the number of Ce^{3+} species formed and the number of O atoms present.

therefore not stable under our in situ DRIFTS conditions. In situ CO DRIFTS during heating of the calcined sample (Section S8 and Figure S12) shows adsorbed CO at 2147 cm^{-1} is oxidized to CO_2 at temperatures much lower than those used for kinetic measurements.

Figure 4b shows the time progression of the DRIFT spectra collected during reduction of CO at 100 °C. After 10 min, only gas-phase CO (2173 cm^{-1}) and CO–Pd^{2+} (2149 cm^{-1}) bands appeared, along with gas-phase CO_2 bands at 2341 cm^{-1} and 2360 cm^{-1}. CO_2 peaks continued to grow as the PdO_x species were reduced and CeO_2 lattice oxygen was consumed, eventually declining as the supply of accessible oxygen was exhausted. As time progressed, bands associated with CO adsorbed to progressively more reduced Pd species emerged at 2106, 2090, and 2070 cm^{-1}. The peak at 2130 cm^{-1} is assigned to CO physisorbed to Ce^{3+}, previously observed during the adsorption of CO on highly reduced ceria.[68,69] At 30 min, peaks in the 1900 cm^{-1} region appeared, a signature for bridge-bonded CO, indicating the onset of Pd clustering.[70,71] As time further progressed, CO_2-associated peaks declined due to slowed CO oxidation due to the depletion of lattice oxygen and desorption

of CO_2 from the catalyst surface, while adsorbed CO peaks remained. After cooling down to room temperature, followed by pressure-swing desorption in He for 60 min, all peaks associated with CO_2 and gas-phase CO disappeared, but CO–Pd bands remained (Figures 4a and S13a) until the temperature exceeded 100 °C during temperature-swing desorption in He (Figure S13b). These results indicate CO binding to in situ-reduced Pd sites is much stronger than to oxidized Pd.

Although Pd single atoms can be reduced by CO to form metallic clusters at 100 °C, they remain oxidized when CO is introduced in the presence of excess oxygen (Figure S13c). Treatment of a 0.03% Pd/CeO_2 catalyst in 2% CO and 20% O_2 in He at 100 °C led to no absorption bands associated with adsorbed CO. Gas-phase CO_2 peaks grow with time on stream. Catalytic CO oxidation requires gas-phase CO to bind to Pd adatoms, with Pd atoms cycling through multiple oxidation states. However, the fraction of Pd atoms with adsorbed CO during CO oxidation catalysis is quite low, as suggested by the high CO reaction order and negative O_2 reaction orders reported in Table 2. We conclude Pd atoms remain in single-
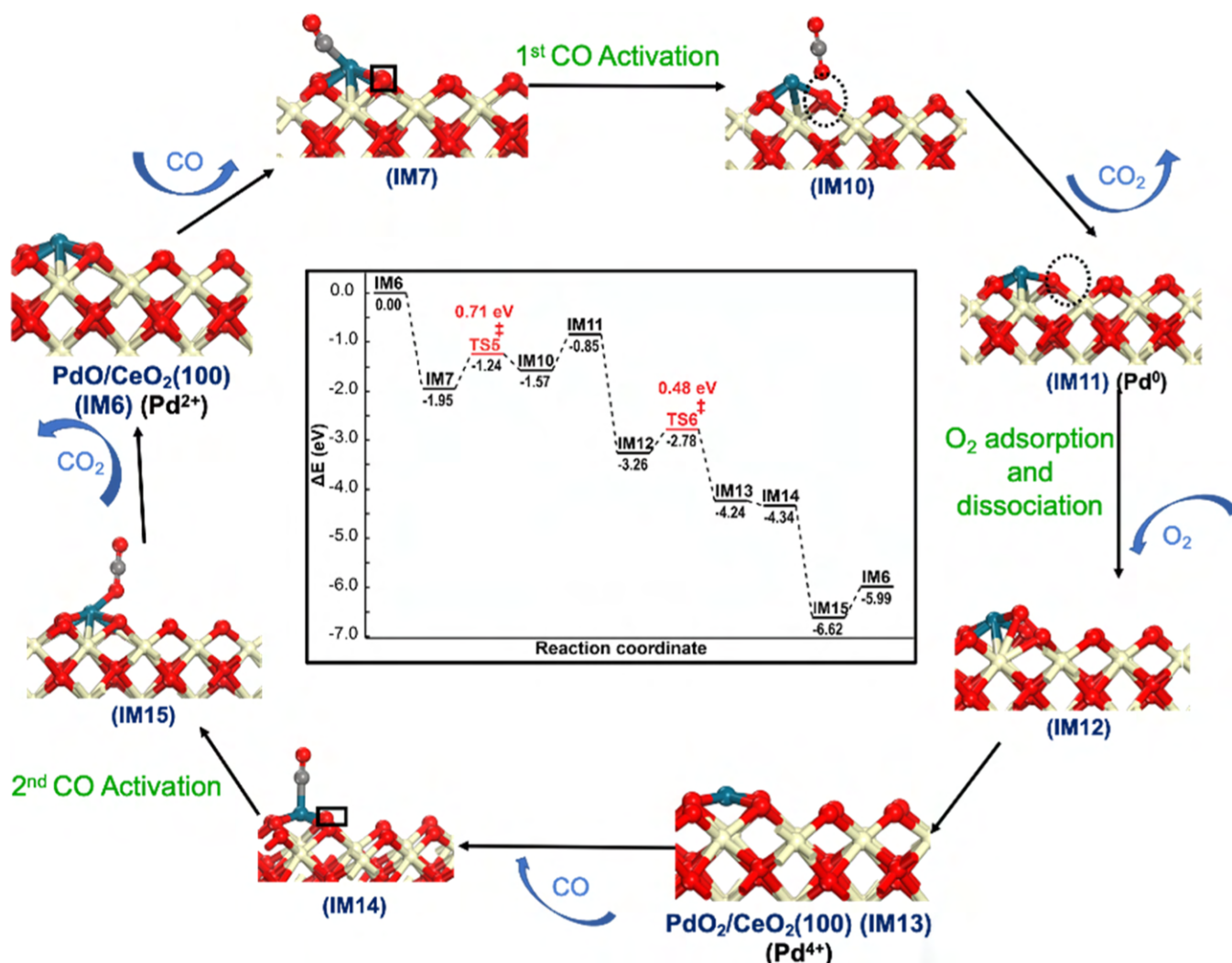
Figure 6. PdO redox cycle $(PdO \leftrightarrow PdO-O_{vac} \leftrightarrow PdO_2 \leftrightarrow PdO)$ with the reaction energy diagram containing reaction energetics and activation barriers for the elementary steps with intermediate structures (IM6, IM7, and IM10−IM15) and TS states (TS5 and TS6). The TS structures are included in Table S11. Reaction energies and barriers for all the elementary steps are also tabulated in Table S10. The black squares indicate the O atoms involved in the activation of CO. The dashed circles indicate an oxygen vacancy formed during CO oxidation. The Pd^{n+} indicated for PdO_x states represents the formal oxidation state of Pd, assigned based on the number of O atoms and Ce^{3+} species present.

atom states during CO oxidation in excess O_2, and the coverage of adsorbed CO is low.

We observed a series of oxidation states of the single Pd atoms in the CO-DRIFTS measurements, the distribution of which was a function of the gas-phase conditions. CO-DRIFTS experiments suggest Pd adatoms can take on 4+, 2+, and 0 formal oxidation states, but no significant coverage of CO is observed during oxidation catalysis, leaving the specific oxidation states that participate in the oxidation catalytic cycle undetermined.

It is common to observe changes in the oxidation states of supported metals under strongly reducing conditions. For example, pretreatment of single-atom Pt/TiO_2 catalysts in 5% H_2/Ar at 250 and 450 °C-reduced Pt species from oxidized Pt^{2+} to cationic $Pt^{\delta+}$ and near-neutral Pt, respectively.[72] Dynamics in the oxidation states of single Pt atoms has been investigated by DFT and first-principles molecular dynamics, where the researchers identified several co-existing oxidation states of Pt species dynamically interconnected.[5] The dynamics of Pd oxidation states has been observed experimentally by Jiang et al., who conducted in situ CO-DRIFTS on 1% Pd/CeO_2 and

identified Pd single atoms clustering into nanoclusters under lean reaction conditions due to the poor stability of deposited Pd single atoms.[65] We did not observe the formation of Pd nanoclusters under O_2-rich reaction conditions, possibly because the Pd weight loading in our sample was significantly lower (0.03%). However, by eliminating the supply of oxygen at reaction temperatures, which gradually led to clustering of the Pd single atoms, we were able to observe multiple oxidation states of Pd.
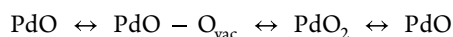
3.5. Pd Oxidation State Dynamics during the CO Redox Cycle/Reaction Mechanism. We used DFT calculations to evaluate elementary reaction energies and activation barriers for CO oxidation catalytic cycles on PdO_x/CeO_2 (100) SACs. As detailed in the Introduction, a "double-cycle" mechanism is used, in which two CO_2 molecules are produced and one O_2 molecule is consumed during each catalytic cycle. The Pd active site oscillates among three formal oxidation states in this mechanism, being reduced by the formation of a "first" CO_2 product, over-oxidized by an O_2 molecule, and then returned to the original oxidation state by forming a "second" CO_2 product. We explored four formal oxidation states for PdO_x

species; this double cycle could occur with either Pd or PdO states as the middle oxidation state in the cycle:

(i) Redox cycle 1, "Pd cycle"

$$Pd \leftrightarrow Pd - O_{vac} \leftrightarrow PdO \leftrightarrow Pd$$

(ii) Redox cycle 2, "PdO cycle"

$$PdO \leftrightarrow PdO - O_{vac} \leftrightarrow PdO_2 \leftrightarrow PdO$$

The first redox cycle is consistent with the DFT analysis of Spezzati et al.,[66] although with slight differences in the specific position/configuration of oxygen atoms involved in the oxidation steps. The reaction energetics and activation barriers are tabulated in Table S10. Intermediate and TS structures for the elementary steps in each cycle are included in Figures 5 and 6 and Table S11, respectively.

The reaction energy diagram for the Pd cycle is shown in Figure 5. The energetics and barriers suggest this redox cycle is viable, with the maximum activation barrier close to the experimental value. The first OC−O bond formation step barrier (0.53 eV), the CO_2 desorption energy (0.69 eV), the second OC−O formation barrier (0.56 eV), and the final oxygen migration step all would have apparent barriers in the range of the experimentally measured barrier. Given the imprecision associated with the use of the GGA + U method,[73] this cycle appears kinetically viable and in reasonable agreement with the experimentally observed activation barrier.

The reaction energy diagram for the "PdO cycle" is shown in Figure 6. Overall, the energetics and barriers render this redox cycle viable, with the maximum barrier close to experimental observations. OC−O formation, CO_2 desorption, and O_2 dissociation all have apparent barriers within 0.1 eV of the experimental barrier. This redox cycle is inconsistent with Spezzati et al.,[66] who reported no adsorption of CO on PdO_2 (contrary to our reported value of −0.10 eV of weak adsorption) and, therefore, argued against the feasibility of this redox cycle.

Either the Pd or PdO cycles represent an operable CO oxidation mechanism on CeO_2-supported Pd SACs. The two cycles can cross-over; for example, a Pd adatom can adsorb CO and proceed through the Pd cycle or adsorb O_2 to form PdO_2 and enter the PdO cycle (Figure S14). There are also more subtle variations in these mechanisms that we explored, differing in whether "lattice O atoms" from the CeO_2 surface or "extra O atoms" adsorbed to the Pd adatom are used for OC−O bond formation from the PdO or PdO_2 states. The participation of lattice O atoms can also influence the O_2 activation process. For example, the Pd state can interact with and dissociate an O_2 molecule directly to form PdO_2 or could appear as a PdO species next to an O vacancy that dissociates O_2 to refill the vacancy and form PdO_2. A detailed description of the various possibilities considered is summarized in the Supporting Information (Section S9.2).

CO oxidation on Pd/CeO_2 (100) SACs may involve redox cycles in which the Pd adatom ranges from PdO_2, PdO, Pd, or Pd adjacent to an O vacancy. Variations in O and CO adsorption energetics with U_{eff} parameters on Ce f or Pd d states suggest the GGA + U level of theory is insufficient to provide quantitative precision to confirm or rule out either of these mechanisms. We, therefore, have used the DFT energetics to help define a plausible set of elementary reaction step sequences (Steps S1−S19 and Table S10) that could represent CO oxidation on Pd SACs. We use the initial DFT energetics within microkinetic models, together with the Bayesian inference, to test these proposed elementary mechanisms against the experimentally measured reaction orders and activation barriers.

3.6. Microkinetic Modeling and Bayesian Inference to Test Elementary CO Oxidation Mechanisms on Pd SACs.

Microkinetic models were constructed as detailed in Section 2.5.2 and utilized within a Bayesian inference framework to reconcile elementary reaction energetics with experimental reaction orders and apparent activation barriers. Although all Pd SACs exhibited similar reaction orders and activation barriers, the microkinetic model was specifically simulated to match values for 0.0056% Pd weight loading (i.e., reaction order CO, reaction order O_2, and activation barrier of 1.30, −0.13, and ~66−67 kJ/mol, respectively) from Table 2. The MKM is run to steady state, determining the steady-state intermediate concentrations and reaction rate. The intermediate concentrations of adsorbate-Pd states are normalized per Pd atom, such that they represent the fraction of Pd single-atom sites in each adsorbate-Pd configuration at steady state. As compared to a mean-field CO oxidation model on an extended surface, all CO and O co-adsorption configurations are enumerated for the single-atom. For example, CO adsorbed on PdO and CO adsorbed on PdO_2 are two distinct states for which steady-state concentrations are determined.

A microkinetic model was first developed containing a basic "double-cycle" mechanism (Table 1). This basic mechanism is inconsistent with the observed experimental CO reaction order greater than 1. This reduced mechanism can be thought of as representing either the Pd cycle or the PdO cycle but does not include cross-over, allowing both cycles to be simultaneously operable. This mechanism is also simple enough that rate expressions can be derived analytically with the assumption of a rate-limiting step and the use of the pseudo-steady-state approximation. Tables S12 and S13 report such analytical analysis, which demonstrates the basic double-cycle mechanism cannot replicate the observed CO reaction order greater than 1. Nonetheless, we also executed Bayesian inference with MKM of this basic mechanism.

The MKM was performed initially with the calculated DFT reaction energetics and barriers for the Pd cycle (Steps S1−S9). Directly using the DFT energetics did not capture the experimentally observed reaction orders in CO or O_2, although the apparent activation barrier matched the experimental value. The CO and O_2 reaction orders and the apparent barrier obtained were 0.01, 0, and 0.62 eV (59.8 kJ/mol), respectively. Similar orders and barriers were obtained when performing the MKM using the DFT energetics for the PdO cycle alone.

MKM including all elementary steps within both the Pd and PdO cycles, as well as the cross-over steps, was then constructed, with elementary energetics populated using DFT data. Again, the DFT-calculated energetics did not result in kinetic behavior in agreement with experimental reaction orders, although the apparent activation barrier was again close to the experiment. The CO and O_2 reaction orders and the apparent barrier obtained were 0.1, 0, and 0.62 eV, respectively. This mismatch with experimental data is attributed to the uncertainties and errors associated with the Pd/CeO_2 terrace model as well as the imprecision in the DFT + U approach.[45,46]

We used a Bayesian inference framework to allow elementary reaction energetics to vary within ranges that approximate the imprecision inherent in the DFT energetics. Bayesian inference was used to calibrate the microkinetic model within both the basic double-cycle mechanism (Steps S1−S9) and the complete reaction network (Steps S1−S19). The detailed definitions of
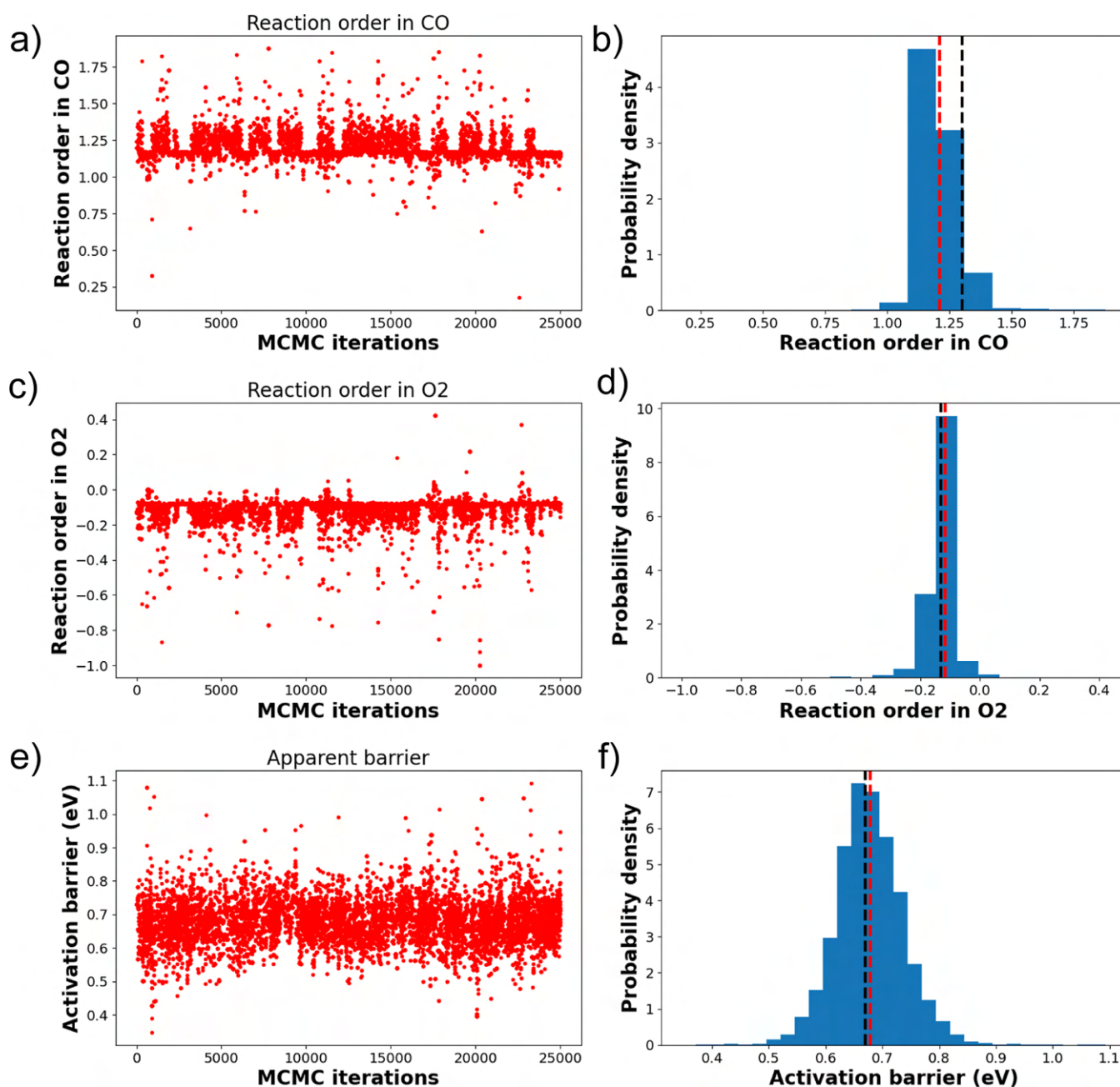
Figure 7. Traces of MKM solutions (calibrated via the Bayesian inference) after sampling the reaction energetic space through 25 000 MCMC iterations (a,c,e) and the corresponding solutions collected in the form of histogram distributions (b,d,f) for the experimental observables. (a,b) Reaction order in CO, (c,d) reaction order in O_2 and (e,f) activation barrier after sampling reaction energetic space for CO oxidation redox cycles (S1–S19) on Pd/CeO_2 (100). The black (–) and red (–) dashed vertical lines in the histograms indicate the experimental and simulated mean values of the reaction orders and activation barriers, respectively.

Bayesian priors, likelihood, and posteriors are detailed in the computational approach for the Bayesian inference in Section S2.7.

The Bayesian inference procedure was unable to find elementary energetics within the basic double-cycle mechanism that match a CO order greater than unity for Pd/CeO_2 SACs. Steady-state reaction orders in CO and O_2 and the apparent reaction barrier were recorded for 10^4 Markov chain Monte Carlo (MCMC) iterations. These iterations sampled the energetic space for the 11 independent reaction energies or barriers, and the resulting apparent reaction orders and barriers are shown in Figure S15. The resulting MKM solutions,

however, only matched the apparent barrier within one standard deviation of error and did not match the experimental reaction orders in CO and O_2. No single MKM solution out of the 10^4 recorded iterations resulted in a reaction order in CO greater than 1. The reaction order in O_2 always stayed slightly positive, in contrast to the experimental negative order (−0.13, Table 2). This suggests the basic double-cycle mechanism (Table 1) is not sufficient to explain the experimentally observed kinetics.

The microkinetic model including both Pd and PdO double cycles, with Bayesian inference, successfully finds elementary reaction energetics that match experimental reaction orders and apparent activation barriers. To match the CO reaction order
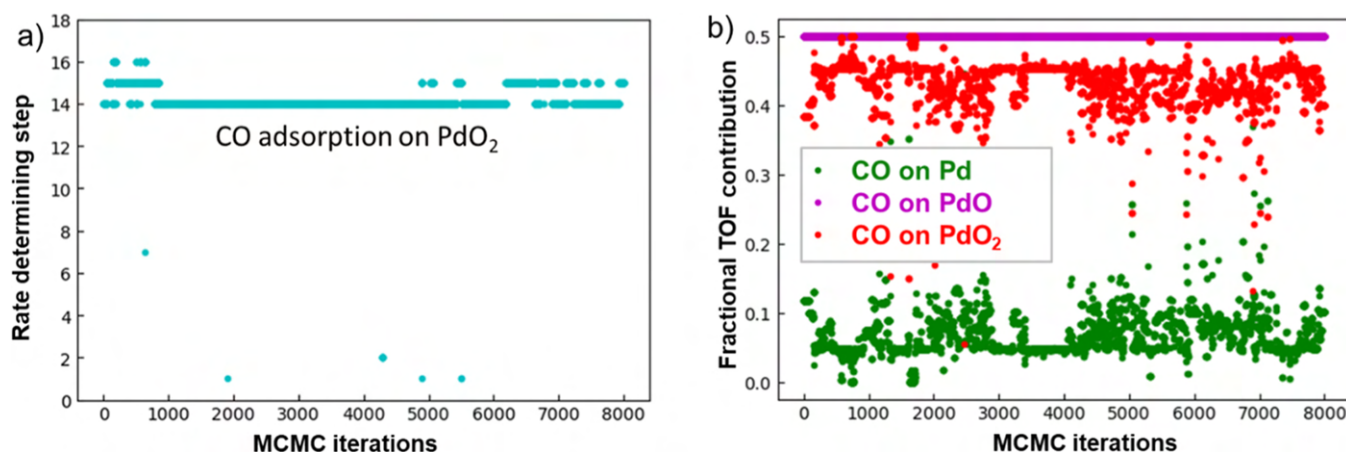
Figure 8. (a) Rate-determining step for the last 8000 MCMC iterations (the step number on the y-axis refers to the elementary steps from Table S10). Step S14 is indicated as the rate-determining step. (b) Individual redox cycles' fractional contribution toward the overall TOF of CO oxidation for the range of MCMC iterations.

greater than unity, the Pd active state oscillates over a span of four formal oxidation states, ranging from PdO_2 to $Pd-O_{vac}$. The space of 26 DFT energetics (17 reaction energies and 9 activation barriers) for the complete reaction network was sampled using Bayesian inference priors to fit to the experimental reaction orders and activation barriers. The posteriors (the sampled energetic space) for all 26 energetics that did fit these observables are shown in Figures S16 and S17. As Bayesian inference sampled the DFT energetic space for the elementary Steps S1−S19, the steady-state reaction orders in CO and O_2 and the apparent reaction barrier were recorded for 25 000 MCMC iterations, and their traces are shown in Figure 7. There is a clear match of the MKM solutions for reaction orders and barriers with the experimental values within one standard deviation of the experimental error. Allowing Pd to oscillate over the larger span of formal Pd oxidation states is necessary to match the experimental orders.

We performed a degree of rate control (DRC) analysis across the last 8000 MCMC iterations from the Bayesian inference sampling. The rate-determining step was determined using the DRC approach[74] and is illustrated in Figure 8a. The probabilistic distribution of the 27-reaction energetics and barrier space (posteriors) showed three different steps (steps 14, 15, and 16) as rate determining across the 8000 iterations, with step 14 (CO adsorption onto the PdO_2 state) being the most frequent rate-determining step. This step determining the rate is consistent with the weak DFT-calculated CO adsorption energy on the Pd^{4+} state (−0.10 eV). Steps 15 (CO oxidation to CO_2 over the PdO_2 state) and 16 (the subsequent CO_2 desorption after step 15) also appear as rate determining in some of the elementary energetic data sets.

The fractional TOF for the different steps that produce CO_2 was also quantified for the same 8000 MCMC iterations (Figure 8b). The fractional TOF contributions show the extent to which Pd, PdO, and PdO_2 states contribute to the amount of CO_2 produced. In the basic Pd double-cycle mechanism, 1/2 of the CO_2 is produced from the Pd state and 1/2 from the PdO state. In the full mechanism, including both Pd and PdO double cycles (Figure 9), CO oxidation in the Pd state contributes only ~5% to the overall CO_2 TOF in a majority of 8000 iterations. CO_2 formed from the PdO state (common to both Pd and PdO cycles), contributes 50%, while CO_2 formed from the PdO_2 state contributes 45% to the total CO_2 TOF. Although these
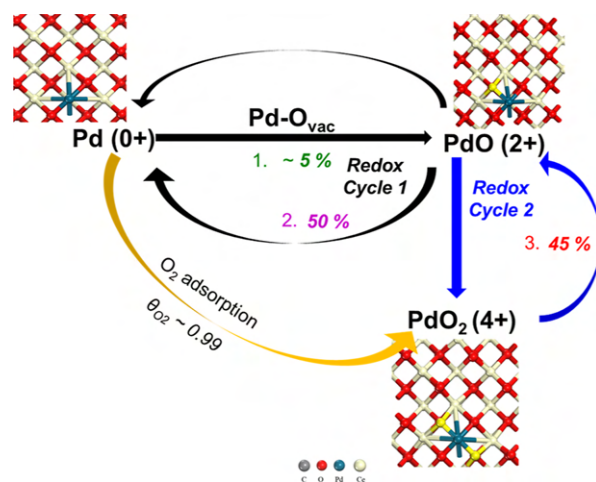
Figure 9. Schematic of the cross-over of Pd and PdO double cycles (redox cycles 1 and 2) observed from MKM reconciled to experimental reaction orders and activation barriers. The indicated fractional TOF contributions (% from Figure 8b) show the extent to which the Pd, PdO, and PdO_2 states contribute to the amount of CO_2 produced. θ_{O_2} represents the steady-state O_2 concentration adsorbed on Pd. The highlighted yellow O atoms in PdO and PdO_2 refer to the extra O (non-lattice) around the Pd site.

fractional TOFs are representative of many of the 8000 MCMC steps, there are also MCMC steps in which these fractional TOFs vary while still matching the experimentally observed kinetics. Clearly, the observation of two reaction orders and an apparent activation barrier does not provide sufficient data to narrow the values of 27 elementary step energetic parameters, and there are multiple solutions that can match the experiment once both Pd and PdO double cycles are included in the mechanism.

We analyzed the steady-state concentrations of reaction intermediates from the same 8000 MCMC iterations. O_2 adsorbed on Pd was the dominant species (~99%) for most sets of elementary energetics. Consequently, the coverage of CO on different Pd states is extremely low, consistent with the absence of adsorbed CO under O_2 + CO co-feed conditions during DRIFTS analysis (Figure S13c). The high coverage of O_2 on Pd is in line with the slight poisoning effect of O_2 (negative O_2 order of −0.13).

CO oxidation across three different Pd states—Pd, PdO, and PdO$_2$—is enabled by the facile variation of Pd oxidation on the CeO$_2$ nanocubes. Our MKM analysis can only conclude whether a mechanism is or is not consistent with the experiment and cannot prove to be an operable mechanism. The active Pd state oscillating only over the basic double-cycle mechanism limits the CO reaction order to 1, whereas the dual double-cycle mechanism allows for higher CO reaction orders and slightly negative O$_2$ reaction orders. This mechanism is also consistent with DFT results demonstrating both Pd and PdO double cycles have viable reaction energetics and DRIFTS results, suggesting a wide range of PdO$_x$/CeO$_2$ nanocube states can be stable and adsorb CO. Under lean conditions, a large fraction of Pd atoms are saturated with oxygen, which decreases their ability to efficiently adsorb CO from the gas phase. As the CO partial pressure increases, greater reduction allows for stronger binding and can accelerate multiple CO$_2$ turnovers before returning to the O-saturated state.

4. CONCLUSIONS

We examined the kinetics of CO oxidation on single-atom Pd/CeO$_2$ catalysts and observed a unique kinetic behavior with a CO reaction order (1.3) greater than unity. The reaction order cannot be explained by the commonly proposed "double-cycle" mechanism for PdO$_x$/CeO$_2$, in which Pd oscillates among only three formal oxidation states ($x - 1$, x, and $x + 1$). By varying the partial pressure of CO and O$_2$ in the feed, a wide range of oxidation states of Pd single atoms were detected by in situ CO-DRIFTS measurements. Although different temperatures and redox conditions were used to observe CO adsorbed to Pd single atoms of variable oxidation states in DRIFTS experiments, we propose these states are accessed dynamically during CO oxidation. The accessibility of Pd single atoms to multiple oxidation states and the dynamics between the states during CO oxidation lead to varying chemical properties of Pd single atoms and the overall activity of the catalyst, which ultimately contributes to the high reaction order in CO. A Bayesian inference-based first-principles microkinetic model was constructed to study the kinetics with the oscillation of PdO$_x$ between different oxidation states. The CO reaction order cannot exceed unity if the reaction follows a redox cycle where Pd oscillates among three oxidation states (e.g., PdO−Pd^0−Pd−O$_{vac}$ or PdO$_2$−PdO−Pd^0). However, when the two redox cycles cross over, Pd accesses four formal oxidation states spanning from +4 (PdO$_2$) to −2 (Pd−O$_{vac}$), and the CO order can exceed unity due to the varying contribution of each redox cycle to the overall kinetics. Our findings unveil the dynamic nature of SACs and provide new insights into the mechanism of redox reaction over single-atom catalysts.

ASSOCIATED CONTENT

ⓢ Supporting Information

The Supporting Information is available free of charge at https://pubs.acs.org/doi/10.1021/acscatal.2c03194.

> Schematic of the reactor for CO oxidation kinetic measurements, computational methods, TEM image of CeO$_2$ nanocubes, approximation of the Pd single-atom regime, DFT model development for CO adsorption to PdO$_x$/CeO$_2$(100), Arrhenius plot of CO oxidation on Pd/CeO$_2$ catalysts, pretreatment for 0.03% Pd/CeO$_2$ for in situ DRIFTS measurements, in situ CO-DRIFTS measurements for single-atom Pd/CeO$_2$, Pd oxidation

state dynamics during the CO redox cycle/reaction mechanism, and MKM and Bayesian inference to test elementary CO oxidation mechanisms on Pd SACs (PDF)

■ AUTHOR INFORMATION

Corresponding Authors

Michael J. Janik − *Department of Chemical Engineering, The Pennsylvania State University, University Park, Pennsylvania 16801, United States;* ⓞ orcid.org/0000-0001-9975-0650; Email: mjanik@psu.edu

Robert M. Rioux − *Department of Chemical Engineering, The Pennsylvania State University, University Park, Pennsylvania 16801, United States; Department of Chemistry, The Pennsylvania State University, University Park, Pennsylvania 16801, United States;* ⓞ orcid.org/0000-0002-6019-0032; Email: rmr189@psu.edu

Authors

Linxi Wang − *Department of Chemical Engineering, The Pennsylvania State University, University Park, Pennsylvania 16801, United States*

Shyam Deo − *Department of Chemical Engineering, The Pennsylvania State University, University Park, Pennsylvania 16801, United States;* ⓞ orcid.org/0000-0002-3590-4398

Ahana Mukhopadhyay − *Department of Chemical Engineering, The Pennsylvania State University, University Park, Pennsylvania 16801, United States*

Nicholas A. Pantelis, II − *Department of Chemical Engineering, The Pennsylvania State University, University Park, Pennsylvania 16801, United States*

Complete contact information is available at:
https://pubs.acs.org/10.1021/acscatal.2c03194

Author Contributions

§L.W. and S.D contributed equally.

Notes

The authors declare no competing financial interest.

■ REFERENCES

(1) Wang, F.; Xia, C.; de Visser, S. P.; Wang, Y. How Does the Oxidation State of Palladium Surfaces Affect the Reactivity and Selectivity of Direct Synthesis of Hydrogen Peroxide from Hydrogen and Oxygen Gases? A Density Functional Study. *J. Am. Chem. Soc.* **2019**, *141*, 901−910.

(2) Ferreira-Aparicio, P.; Bachiller-Baeza, B.; Rodríguez-Ramos, I.; Guerrero-Ruiz, A.; Fernández-García, M. Correlation between metal oxidation state and catalytic activity: hydrogenation of crotonaldehyde over Rh catalysts. *Catal. Lett.* **1997**, *49*, 163−167.

(3) Ameur, N.; Bedrane, S.; Bachir, R.; Choukchou-Braham, A. Influence of nanoparticles oxidation state in gold based catalysts on the product selectivity in liquid phase oxidation of cyclohexene. *J. Mol. Catal. A: Chem.* **2013**, *374–375*, 1−6.

(4) Cuenya, B. Synthesis and catalytic properties of metal nanoparticles: Size, shape, support, composition, and oxidation state effects. *Thin Solid Films* **2010**, *518*, 3127−3150.

(5) Daelman, N.; Capdevila-Cortada, M.; López, N. Dynamic charge and oxidation state of Pt/CeO2 single-atom catalysts. *Nat. Mater.* **2019**, *18*, 1215−1221.

(6) Shin, S.; Kim, J.; Park, S.; Kim, H. E.; Sung, Y. E.; Lee, H. Changes in the oxidation state of Pt single-atom catalysts upon removal of chloride ligands and their effect for electrochemical reactions. *Chem. Commun.* **2019**, *55*, 6389−6392.

(7) Jeong, H.; Shin, D.; Kim, B. S.; Bae, J.; Shin, S.; Choe, C.; Han, J. W.; Lee, H. Controlling the Oxidation State of Pt Single Atoms for Maximizing Catalytic Activity. *Angew. Chem., Int. Ed.* **2020**, *59*, 20691−20696.

(8) Senftle, T. P.; van Duin, A. C. T.; Janik, M. J. Methane Activation at the Pd/CeO2 Interface. *ACS Catal.* **2017**, *7*, 327−332.

(9) Senftle, T. P.; van Duin, A. C. T.; Janik, M. J. Role of Site Stability in Methane Activation on PdxCe1-xO delta Surfaces. *ACS Catal.* **2015**, *5*, 6187−6199.

(10) Zhang, L. H.; Mathew, S.; Hessels, J.; Reek, J. N. H.; Yu, F. S. Homogeneous Catalysts Based on First-Row Transition-Metals for Electrochemical Water Oxidation. *ChemSusChem* **2021**, *14*, 234−250.

(11) Joya, K. S.; Subbaiyan, N. K.; D'Souza, F.; de Groot, H. J. M. Surface-Immobilized Single-Site Iridium Complexes for Electrocatalytic Water Splitting. *Angew. Chem., Int. Ed.* **2012**, *51*, 9601−9605.

(12) Blakemore, J. D.; Schley, N. D.; Balcells, D.; Hull, J. F.; Olack, G. W.; Incarvito, C. D.; Eisenstein, O.; Brudvig, G. W.; Crabtree, R. H. Half-Sandwich Iridium Complexes for Homogeneous Water-Oxidation Catalysis. *J. Am. Chem. Soc.* **2010**, *132*, 16017−16029.

(13) Zhang, L.-H.; Mathew, S.; Hessels, J.; Reek, J. N. H.; Yu, F. Homogeneous Catalysts Based on First-Row Transition-Metals for Electrochemical Water Oxidation. *ChemSusChem* **2021**, *14*, 234−250.

(14) Zhang, X.; Liu, H.; An, P.; Shi, Y.; Han, J.; Yang, Z.; Long, C.; Guo, J.; Zhao, S.; Zhao, K.; Yin, H.; Zheng, L.; Zhang, B.; Liu, X.; Zhang, L.; Li, G.; Tang, Z. Delocalized electron effect on single metal sites in ultrathin conjugated microporous polymer nanosheets for boosting CO2 cycloaddition. *Sci. Adv.* **2020**, *6*, No. eaaz4824.

(15) Cuenya, B. R. Synthesis and catalytic properties of metal nanoparticles: Size, shape, support, composition, and oxidation state effects. *Thin Solid Films* **2010**, *518*, 3127−3150.

(16) Campbell, C. T. Electronic perturbations. *Nat. Chem.* **2012**, *4*, 597.

(17) Bruix, A.; Rodriguez, J. A.; Ramírez, P. J.; Senanayake, S. D.; Evans, J.; Park, J. B.; Stacchiola, D.; Liu, P.; Hrbek, J.; Illas, F. A New Type of Strong Metal−Support Interaction and the Production of H2 through the Transformation of Water on Pt/CeO2(111) and Pt/CeOx/TiO2(110) Catalysts. *J. Am. Chem. Soc.* **2012**, *134*, 8968−8974.

(18) Mourdikoudis, S.; Pallares, R. M.; Thanh, N. T. K. Characterization techniques for nanoparticles: comparison and complementarity upon studying nanoparticle properties. *Nanoscale* **2018**, *10*, 12871−12934.

(19) Pedersen, A. F.; Escudero-Escribano, M.; Sebok, B.; Bodin, A.; Paoli, E.; Frydendal, R.; Friebel, D.; Stephens, I. E. L.; Rossmeisl, J.; Chorkendorff, I.; Nilsson, A. Operando XAS Study of the Surface Oxidation State on a Monolayer IrOx on RuOx and Ru Oxide Based Nanoparticles for Oxygen Evolution in Acidic Media. *J. Phys. Chem. B* **2018**, *122*, 878−887.

(20) Fock, J.; Bogart, L. K.; González-Alonso, D.; Espeso, J. I.; Hansen, M. F.; Varón, M.; Frandsen, C.; Pankhurst, Q. A. On the 'centre of gravity' method for measuring the composition of magnetite/maghemite mixtures, or the stoichiometry of magnetite-maghemite solid solutions, via ^{57}Fe Mössbauer spectroscopy. *J. Phys. D: Appl. Phys.* **2017**, *50*, 265005.

(21) Daelman, N.; Capdevila-Cortada, M.; López, N. Dynamic charge and oxidation state of Pt/CeO2 single-atom catalysts. *Nat. Mater.* **2019**, *18*, 1215−1221.

(22) Toyoshima, R.; Ueda, K.; Koda, Y.; Kodama, H.; Sumida, H.; Mase, K.; Kondoh, H. In situ AP-XPS study on reduction of oxidized Rh catalysts under CO exposure and catalytic reaction conditions. *J. Phys. D: Appl. Phys.* **2021**, *54*, 204005.

(23) Vlahovic, F.; Gruden, M.; Stepanovic, S.; Swart, M. Density functional approximations for consistent spin and oxidation states of oxoiron complexes. *Int. J. Quantum Chem.* **2020**, *120*, No. e26121.

(24) Venezia, A. M. X-ray photoelectron spectroscopy (XPS) for catalysts characterization. *Catal. Today* **2003**, *77*, 359−370.

(25) Bazin, D.; Rehr, J. J. Limits and Advantages of X-ray Absorption Near Edge Structure for Nanometer Scale Metallic Clusters. *J. Phys. Chem. B* **2003**, *107*, 12398−12402.

(26) Alexopoulos, K.; Wang, Y.; Vlachos, D. G. First-Principles Kinetic and Spectroscopic Insights into Single-Atom Catalysis. *ACS Catal.* **2019**, *9*, 5002−5010.

(27) Spezzati, G.; Su, Y.; Hofmann, J. P.; Benavidez, A. D.; DeLaRiva, A. T.; McCabe, J.; Datye, A. K.; Hensen, E. J. M. Atomically dispersed Pd-O species on CeO2(111) as highly active sites for low-temperature CO oxidation. *ACS Catal.* **2017**, *7*, 6887−6891.

(28) Lu, Y.; Wang, J.; Yu, Y.; Kovarik, L.; Zhang, X.; Hoffman, A. S.; Gallo, A.; Bare, S. R.; Sokaras, D.; Kroll, T.; Dagle, V.; Xin, H.; Karim, A. M. Identification of the active complex for CO oxidation over single-atom Ir-on-MgAl2O4 catalysts. *Nat. Catal.* **2019**, *2*, 149−156.

(29) Jiang, D.; Wan, G.; García-Vargas, C. E.; Li, L.; Pereira-Hernández, X.; Wang, C.; Wang, Y. Elucidation of the Active Sites in Single-Atom Pd1/CeO2 Catalysts for Low-Temperature CO Oxidation. *ACS Catal.* **2020**, *10*, 11356−11364.

(30) Zhao, E. W.; Zheng, H. B.; Zhou, R. H.; Hagelin-Weaver, H. E.; Bowers, C. R. Shaped Ceria Nanocrystals Catalyze Efficient and Selective Para-Hydrogen-Enhanced Polarization. *Angew. Chem., Int. Ed.* **2015**, *54*, 14270−14275.

(31) Wang, R.; Dangerfield, R. Seed-mediated synthesis of shape-controlled CeO2 nanocrystals. *RSC Adv.* **2014**, *4*, 3615−3620.

(32) Keels, J. M.; Chen, X.; Karakalos, S.; Liang, C.; Monnier, J. R.; Regalbuto, J. R. Aqueous-Phase Hydrogenation of Succinic Acid Using Bimetallic Ir−Re/C Catalysts Prepared by Strong Electrostatic Adsorption. *ACS Catal.* **2018**, *8*, 6486−6494.

(33) D'Souza, L.; Regalbuto, J. R. Strong electrostatic adsorption for the preparation of Pt/Co/C and Pd/Co/C bimetallic electrocatalysts. *Stud. Surf. Sci. Catal.* **2010**, *175*, 715−718.

(34) Kresse, G.; Furthmüller, J. Efficient iterative schemes for ab initio total-energy calculations using a plane-wave basis set. *Phys. Rev. B: Condens. Matter Mater. Phys.* **1996**, *54*, 11169−11186.

(35) Kresse, G.; Hafner, J. Ab initio molecular dynamics for liquid metals. *Phys. Rev. B: Condens. Matter Mater. Phys.* **1993**, *47*, 558−561.

(36) Perdew, J. P.; Wang, Y. Accurate and simple analytic representation of the electron-gas correlation energy. *Phys. Rev. B: Condens. Matter Mater. Phys.* **1992**, *45*, 13244−13249.

(37) Blöchl, P. E. Projector augmented-wave method. *Phys. Rev. B: Condens. Matter Mater. Phys.* **1994**, *50*, 17953−17979.

(38) Dudarev, S. L.; Botton, G. A.; Savrasov, S. Y.; Humphreys, C. J.; Sutton, A. P. Electron-energy-loss spectra and the structural stability of nickel oxide: An LSDA+U study. *Phys. Rev. B: Condens. Matter Mater. Phys.* **1998**, *57*, 1505−1509.

(39) Nolan, M.; Parker, S. C.; Watson, G. W. The electronic structure of oxygen vacancy defects at the low index surfaces of ceria. *Surf. Sci.* **2005**, *595*, 223−232.

(40) Monkhorst, H. J.; Pack, J. D. Special points for Brillouin-zone integrations. *Phys. Rev. B: Solid State* **1976**, *13*, 5188−5192.

(41) Henkelman, G.; Uberuaga, B. P.; Jónsson, H. A climbing image nudged elastic band method for finding saddle points and minimum energy paths. *J. Chem. Phys.* **2000**, *113*, 9901−9904.

(42) Henkelman, G.; Jónsson, H. A dimer method for finding saddle points on high dimensional potential surfaces using only first derivatives. *J. Chem. Phys.* **1999**, *111*, 7010−7022.

(43) Kümmerle, E. A.; Heger, G. The Structures of C−Ce2O3+δ, Ce7O12, and Ce11O20. *J. Solid State Chem.* **1999**, *147*, 485−500.

(44) Puchin, V. E.; Puchina, A. V.; Huisinga, M.; Reichling, M. Theoretical modelling of steps on the CaF2(111) surface. *J. Phys.: Condens. Matter* **2001**, *13*, 2081−2094.

(45) Kulik, H. J. Perspective: Treating electron over-delocalization with the DFT+U method. *J. Chem. Phys.* **2015**, *142*, 240901.

(46) Kulik, H. J.; Cococcioni, M.; Scherlis, D. A.; Marzari, N. Density Functional Theory in Transition-Metal Chemistry: A Self-Consistent Hubbard U Approach. *Phys. Rev. Lett.* **2006**, *97*, 103001.

(47) Jaynes, E. T.*Probability Theory: The Logic of Science*; Cambridge University Press: Cambridge, 2003.

(48) Szanyi, J.; Goodman, D. W. CO Oxidation on Palladium. 1. A Combined Kinetic-Infrared Reflection Absorption Spectroscopic Study of Pd(100). *J. Phys. Chem.* **1994**, *98*, 2972−2977.

(49) Gaudet, J. R.; de la Riva, A.; Peterson, E. J.; Bolin, T.; Datye, A. K. Improved Low-Temperature CO Oxidation Performance of Pd Supported on La-Stabilized Alumina. *ACS Catal.* **2013**, *3*, 846−855.

(50) Liu, L.; Zhou, F.; Wang, L.; Qi, X.; Shi, F.; Deng, Y. Low-temperature CO oxidation over supported Pt, Pd catalysts: Particular role of FeOx support for oxygen supply during reactions. *J. Catal.* **2010**, *274*, 1−10.

(51) Kim, H. Y.; Henkelman, G. CO Oxidation at the Interface of Au Nanoclusters and the Stepped-CeO2(111) Surface by the Mars-van Krevelen Mechanism. *J. Phys. Chem. Lett.* **2013**, *4*, 216−221.

(52) Wang, J.; Wang, M.; Li, W.; Qiao, W.; Long, D.; Ling, L. Application of polyethylenimine-impregnated solid adsorbents for direct capture of low-concentration CO2. *AIChE J.* **2015**, *61*, 972−980.

(53) Lang, W.; Laing, P.; Cheng, Y.; Hubbard, C.; Harold, M. P. Co-oxidation of CO and propylene on Pd/CeO2-ZrO2 and Pd/Al2O3 monolith catalysts: A light-off, kinetics, and mechanistic study. *Appl. Catal., B* **2017**, *218*, 430−442.

(54) Brandt, B.; Schalow, T.; Laurin, M.; Schauermann, S.; Libuda, J.; Freund, H. J. Oxidation, reduction, and reactivity of supported Pd nanoparticles: mechanism and microkinetics. *J. Phys. Chem. C* **2007**, *111*, 938−949.

(55) Muravev, V.; Spezzati, G.; Su, Y.-Q.; Parastaev, A.; Chiang, F.-K.; Longo, A.; Escudero, C.; Kosinov, N.; Hensen, E. J. M. Interface dynamics of Pd−CeO2 single-atom catalysts during CO oxidation. *Nat. Catal.* **2021**, *4*, 469−478.

(56) Alexopoulos, K.; Vlachos, D. G. Surface chemistry dictates stability and oxidation state of supported single metal catalyst atoms. *Chem. Sci.* **2020**, *11*, 1469−1477.

(57) Kuendig, E. P.; McIntosh, D.; Moskovits, M.; Ozin, G. A. Binary carbonyls of platinum, Pt(CO)n (where n = 1-4). Comparative study of the chemical and physical properties of M(CO)n (where M = nickel, palladium, or platinum; n = 1-4). *J. Am. Chem. Soc.* **1973**, *95*, 7234−7241.

(58) Wovchko, E. A.; Yates, J. T. Nitrogen Chemisorption on the Coordinatively Unsaturated Rh Site on Al2O3. *J. Am. Chem. Soc.* **1996**, *118*, 10250−10256.

(59) Miessner, H. Surface Chemistry in a Zeolite Matrix. Well-Defined Dinitrogen Complexes of Rhodium Supported on Deal-uminated Y Zeolite. *J. Am. Chem. Soc.* **1994**, *116*, 11522−11530.

(60) Spoto, G.; Zecchina, A.; Bordiga, S.; Ricchiardi, G.; Martra, G.; Leofanti, G.; Petrini, G. Cu(I)-ZSM-5 zeolites prepared by reaction of H-ZSM-5 with gaseous CuCl: Spectroscopic characterization and reactivity towards carbon monoxide and nitric oxide. *Appl. Catal., B* **1994**, *3*, 151−172.

(61) Tessier, D.; Rakai, A.; Bozon-Verduraz, F. In Spectroscopic Study of the Interaction of Carbon Monoxide with Cationic and Metallic Palladium in Palladium-Alumina Catalysts. *J. Chem. Soc., Faraday Trans.* **1992**, *88*, 741−749.

(62) Jaatinen, S.; Salo, P.; Alatalo, M.; Kokko, K. Effect of the electronic structure on CO oxidation on Pd doped Ag(111). *Surf. Sci.* **2004**, *566−568*, 1063−1066.

(63) Martin, N. M.; Van den Bossche, M.; Grönbeck, H.; Hakanoglu, C.; Zhang, F.; Li, T.; Gustafson, J.; Weaver, J. F.; Lundgren, E. CO Adsorption on Clean and Oxidized Pd(111). *J. Phys. Chem. C* **2014**, *118*, 1118−1128.

(64) Boronin, A. I.; Slavinskaya, E. M.; Danilova, I. G.; Gulyaev, R. V.; Amosov, Y. I.; Kuznetsov, P. A.; Polukhina, I. A.; Koscheev, S. V.; Zaikovskii, V. I.; Noskov, A. S. Investigation of palladium interaction with cerium oxide and its state in catalysts for low-temperature CO oxidation. *Catal. Today* **2009**, *144*, 201−211.

(65) Jiang, D.; Wan, G.; García-Vargas, C. E.; Li, L.; Pereira-Hernández, X. I.; Wang, C.; Wang, Y. Elucidation of the Active Sites in Single-Atom Pd1/CeO2 Catalysts for Low-Temperature CO Oxidation. *ACS Catal.* **2020**, *10*, 11356−11364.

(66) Spezzati, G.; Benavidez, A. D.; DeLaRiva, A. T.; Su, Y.; Hofmann, J. P.; Asahina, S.; Olivier, E. J.; Neethling, J. H.; Miller, J. T.; Datye, A. K.; Hensen, E. J. M. CO oxidation by Pd supported on CeO2(100) and CeO2(111) facets. *Appl. Catal., B* **2019**, *243*, 36−46.

(67) Martin, N. M.; Van den Bossche, M.; Grönbeck, H.; Hakanoglu, C.; Zhang, F.; Li, T.; Gustafson, J.; Weaver, J. F.; Lundgren, E. CO Adsorption on Clean and Oxidized Pd(111). *J. Phys. Chem. C* **2014**, *118*, 1118−1128.

(68) Binet, C.; Daturi, M.; Lavalley, J. C. IR study of polycrystalline ceria properties in oxidised and reduced states. *Catal. Today* **1999**, *50*, 207−225.

(69) Bozon-Verduraz, F.; Bensalem, A. IR Studies of Cerium Dioxide: Influence of Impurities and Defects. *J. Chem. Soc., Faraday Trans.* **1994**, *90*, 653−657.

(70) Szanyi, J.; Kwak, J. H. Dissecting the steps of CO2 reduction: 2. The interaction of CO and CO2 with Pd/γ-Al2O3: An in situ FTIR study. *Phys. Chem. Chem. Phys.* **2014**, *16*, 15126−15138.

(71) Föttinger, K.; Emhofer, W.; Lennon, D.; Rupprechter, G. Adsorption and Reaction of CO on (Pd-)Al2O3 and (Pd-)ZrO2: Vibrational Spectroscopy of Carbonate Formation. *Top. Catal.* **2017**, *60*, 1722−1734.

(72) DeRita, L.; Resasco, J.; Dai, S.; Boubnov, A.; Thang, H. V.; Hoffman, A. S.; Ro, I.; Graham, G. W.; Bare, S. R.; Pacchioni, G.; Pan, X.; Christopher, P. Structural evolution of atomically dispersed Pt catalysts dictates reactivity. *Nat. Mater.* **2019**, *18*, 746−751.

(73) Himmetoglu, B.; Floris, A.; de Gironcoli, S.; Cococcioni, M. Hubbard-corrected DFT energy functionals: The LDA+U description of correlated systems. *Int. J. Quantum Chem.* **2014**, *114*, 14−49.

(74) Campbell, C. T. The Degree of Rate Control: A Powerful Tool for Catalysis Research. *ACS Catal.* **2017**, *7*, 2770−2779.

■ NOTE ADDED AFTER ASAP PUBLICATION

The version of this paper that was published ASAP October 11, 2022, contained a spelling error in the name of author Ahana Mukhopadhyay. The corrected version was reposted October 11, 2022.